

J.P.S. Bizarro, F. Köchl, I. Voitsekhovitch
and JET EFDA contributors

Modelling the Ohmic L-mode Ramp-down Phase of JET Hybrid Pulses Using JETTO with Bohm-Gyro-Bohm Transport

“This document is intended for publication in the open literature. It is made available on the understanding that it may not be further circulated and extracts or references may not be published prior to publication of the original when applicable, or without the consent of the Publications Officer, EFDA, Culham Science Centre, Abingdon, Oxon, OX14 3DB, UK.”

“Enquiries about Copyright and reproduction should be addressed to the Publications Officer, EFDA, Culham Science Centre, Abingdon, Oxon, OX14 3DB, UK.”

The contents of this preprint and all other JET EFDA Preprints and Conference Papers are available to view online free at www.iop.org/Jet. This site has full search facilities and e-mail alert options. The diagrams contained within the PDFs on this site are hyperlinked from the year 1996 onwards.

Modelling the Ohmic L-mode Ramp-down Phase of JET Hybrid Pulses Using JETTO with Bohm-Gyro-Bohm Transport

J.P.S. Bizarro¹, F. Köchl², I. Voitsekhovitch³
and JET EFDA contributors*

JET-EFDA, Culham Science Centre, OX14 3DB, Abingdon, UK

¹*Associação EURATOM-IST, Instituto de Plasmas e Fusão Nuclear,
Instituto Superior Técnico, Universidade Técnica de Lisboa, 1049-001 Lisboa, Portugal*

²*Association EURATOM-ÖAW/ATI, Atominstitut, TU Wien, 1020 Vienna, Austria*

³*EURATOM-CCFE Fusion Association, Culham Science Centre, OX14 3DB, Abingdon, OXON, UK*

* See annex of F. Romanelli et al, “Overview of JET Results”,
(24th IAEA Fusion Energy Conference, San Diego, USA (2012)).

ABSTRACT

The empirical Bohm-gyro-Bohm (BgB) transport model implemented in the JETTO code is used to predictively simulate the purely Ohmic (OH), L-mode current-ramp-down phase of three JET hybrid pulses, which combine two different ramp rates with two different electron densities (at the beginning of the ramp). The modelling is discussed, namely the strategy to reduce as much as possible the number of free parameters used to benchmark the model predictions against the experimental results. Hence, by keeping the gas puffing rate as measured whilst tuning the line-average electron density via the recycling coefficient (which in the modelling is taken at the separatrix instead of the wall), it is shown that the BgB model reproduces well the experimental data, as far as both average quantities (plasma internal inductance, linear-average electron density and volume average electron temperature) and profiles (electron density and temperature) are concerned, with relative errors remaining mostly below 20%. The sensitiveness with respect to the recycling coefficient, the ion effective charge and the energy of neutrals entering the plasma through the separatrix are assessed, being also shown the need for a proper sawtooth model if experimental results are to be reproduced. The strong non-linear coupling in a OH plasma between density, temperature and current (essentially via interplay between the power-balance equation, Joule's heating with a temperature-dependent resistivity and the dependence of BgB transport coefficients on profile gradients) is put in evidence and analyzed in light of modelling results. It is still inferred from the modelling that the real value of the recycling coefficient at the separatrix (basically, the so-called fuelling efficiency times the actual recycling coefficient at the wall) must become close to one in the final stages of the discharges, when the gas puffing is switched off and so recycling comes to be the only source of particles. If the wall recycling remains close to one (as standard for tokamaks), this may indicate that the fuelling efficiency also approaches unity, apparently consistent with the observed fact that the plasma is pushed towards the machine wall at the end of the current ramps.

1. INTRODUCTION

The simulation and modelling of plasma scenarios has always been a major activity in magnetic fusion research and one which, particularly in view of ITER, has seen a significant increase in the latter years and has become mostly focused on integrated tokamak modelling [1, 2, 3, 4, 5, 6, 7, 8, 10, 11, 12, 13, 14, 15, 16, 17, 18, 19, 20, 21, 22, 23, 24, 25]. For their most part, tokamak modelling activities have addressed the so-called ramp-up and at-top phases of tokamak pulses, and not that much attention has been paid to the termination of tokamak discharges, when the plasma current is ramped down to zero. The ramp-down, current-decay phase of a tokamak pulse must not be regarded as a matter of lesser interest, and the modelling effort allocated to it must not be less (in proportion at least) than that which is dedicated to the rest of the discharge. Indeed, and as long as tokamak operation is not steady state, pulses should be safely terminated and so appropriate ramp-down modelling must become available, inasmuch as additional concerns arise about such things as disruption, stability, and volt-second saving [13, 14, 18, 20, 25, 26, 27, 28, 29, 30]. Reflecting

the importance that ramp-down simulation and modelling has acquired, various reports on the subject have started to appear in the literature [12, 13, 14, 18, 20, 25], yet all of them (but one [25]), taking prescribed plasma density profiles (i.e., predictively evolving the current density and temperature profiles only) and none giving a full account of how well the transport model chosen fares when used to fully predict ramp-down data from actual experiments (i.e., to simultaneously predict the time evolution of density, temperature, and current profiles). The main purpose of this paper is precisely to provide a first, comprehensive report on how one of such transport models, the Bohm{gyro-Bohm (BgB) model implemented in the JETTO code [1, 2, 3, 4, 5], is bench marked on the purely Ohmic (OH) L mode ramp-down phase of JET hybrid discharges [25, 31]. This type of discharges has been chosen not only because of its importance for the JET programme aiming at the qualification of ITER operating scenarios, the hybrid scenario being a promising route for ITER to achieve fusion-grade performance at lower plasma current and, therefore, longer pulse duration, but also to complement the considerable effort that has been put in the understanding and modelling of such a scenario [25, 31].

The empirical BgB model is well-known and has been applied (here and there with a few adjustments) to a wide variety of situations and with a fair amount of success, not least because of the rapidity with which it allows transport simulations to be performed and still because it is not hindered by the numerical stability problems that often plague first-principles codes [1, 2, 3, 4, 5, 6, 8, 10, 12, 17, 20, 22, 24, 25]. Although reference to its use and test in the simulation of L-mode ramp-down plasmas in JET can be found [12, 25], no comprehensive analysis has yet been published on the benchmarking of the BgB model on the terminal phase of tokamak discharges. More recently, a detailed investigation of how the BgB and other transport models are capable to reproduce the experimental data in ASDEX Upgrade current ramps has come out [24], but it has actually been concerned solely with current ramp-up and only temperatures and current density have been predicted, whilst plasma density has been treated interpretatively. Therefore, the BgBmodel (in its original L-mode form [1], albeit with slightly modified tuned coefficients) will be used herein to simulate the final, ramp-down phase of three JET hybrid shots (Pulse No: 75225, Pulse No: 76793 and Pulse No: 77922), which combine different current rampdown rates and different plasma densities. Using as input as much of the experimental data as possible (e.g., radiated power, effective ion charge, gas puffing rate and initial and boundary conditions for density, temperature and current), the BgB model in JETTO is used to evolve in time the profiles for plasma and current densities and electron and ion temperatures. A further motivation for the present work comes from the reporting that simulations of current ramp-down including the so-called H- to L-mode back transition show an overestimated density after the latter has occurred (when the plasma is already in L-mode or in OH) [32], which can be attributed to some inaccuracy either in the BgB transport model, in the density-dependent power threshold for the back transition or in assumptions for the effective particle recycling. Hence, to check the capability of the BgB model to accurately predict the density and temperature evolution during the current ramp-down phase, this model has been

applied to plasmas where the H to L back transition occurs at the end of the current plateau (before the beginning of the ramp-down phase), so it does not become an issue in the modelling of the subsequent current ramp, which takes place entirely in a OH plasma. As for the way this paper is organized, the experimental scenario is described in section 2, where a brief discussion is also given on which diagnostics and signals are used in the analysis, whilst in section 3 details of the simulation model are presented, with the L-mode BgB equations within JETTO being recalled for completeness and the strategy of the benchmarking being outlined. In section 4, the results of the comparison between predictive simulations and experimental data are given and discussed, the sensitivity of model predictions a summary being provided and conclusions being drawn in section 5.

2. EXPERIMENTAL SCENARIO

2.1 DISCHARGE CHARACTERISTICS.

As stated in section 1, three hybrid discharges representative of JET (Pulse No's: 75225, 76793 and 77922) have been selected for the modelling of the current ramp-down phase, which discharges have been performed at different reference magnetic field B_{ref} , electron density n_e and plasma shape during the current flat-top. The hybrid phase in these discharges is terminated when the injected neutral-beam power is switched off (during the current plateau), the ramp in plasma current I_p starting in OH plasmas 5–7s later, with I_p being ramped from $I_p \approx 1.7\text{MA}$ down to $I_p \approx 0.4\text{--}0.5\text{MA}$ at a rate of $dI_p/dt \approx 0.17\text{--}0.21\text{MA/s}$. The two discharges with the faster ramp-down rate ($dI_p/dt \approx 0.21\text{MA/s}$ for Pulse No's: 75225 and 77922) start from different linear-average electron densities \bar{n}_e at the beginning of the ramp-down (respectively, $\bar{n}_e \approx 0.8$ and $1.1 \times 10^{19} \text{ m}^{-3}$), whereas the two low-density discharges ($\bar{n}_e \approx 0.8 \times 10^{19} \text{ m}^{-3}$ for Pulse No: 75225 and Pulse No: 76793) present different ramp-down rates (respectively, $dI_p/dt \approx 0.21$ and 0.17MA/s). The toroidal magnetic field (which is lower for Pulse No: 75225 and Pulse No: 76793) reduces by 43–46% during ramp-down, whilst the plasma shape slightly evolves, approaching the wall at the top and inner part of the chamber at the end of the ramp, with the plasma volume exhibiting little variation (3.0–3.6%, except for a 7% volume reduction at the very end of the ramp-down for Pulse No: 75225). This volume reduction is a common feature seen when, in the course of the current ramp-down, I_p becomes low enough so that the plasma shape cannot be controlled well and a so-called soft-stop procedure becomes into effect (typically around $t \approx 22.2\text{--}23.5\text{s}$) to terminate the discharge safely [33], this very final stage of the discharge being often accompanied by a degradation in the quality of the measured data. Soft X-ray measurements are available for Pulse No: 76793 and Pulse No: 77922 only and show small sawteeth that become more frequent until disappearing nearly at the end of the ramp (at $t \approx 21\text{--}22\text{s}$ and lasting longer for the latter shot), their period decreasing from 0.1 to 0.05s while their $\underline{\text{inversion radius}}$ goes from 0.25 to 0.3 (in the flux coordinate ϵ defined later), as inferred from electron cyclotron emission (ECE) data. The scenarios for the three discharges are graphically summarized in figure 1, where time traces are shown not only for I_p , B_{ref} and n_e , but also for plasma internal inductance l_i (as given by equilibrium reconstruction using EFIT [34, 35]) and volume-averaged electron temperature $\langle T_e \rangle$.

2.2 EXPERIMENTAL DATA.

Measurements of electron density and temperature have essentially relied on the high-resolution Thomson scattering (HRTS) diagnostic, whose resolutions in space and time are of about 1.7cm and 50ms, respectively. However, and since the HRTS line of sight is below the mid-plane and so does not cover the plasma center, n_e measurements in this region have been performed with a Thomson scattering LIDAR system with a spatial resolution of 5cm and temporal resolution of 250ms. In addition to HRTS, an ECE diagnostic covering the whole plasma, with space and time resolutions of 5cm and 22ms, respectively, has been used for T_e measurements. These have been the experimental data which have been fitted to obtain the initial n_e and T_e profiles (with the initial ion temperature profile T_i taken identical to T_e). In OH plasmas, where charge exchange (CX) measurements of the profile for the effective ion charge Z_{eff} are not available, bremsstrahlung data for vertical line-averaged Z_{eff} have been used (considering Carbon impurity only) and a radially at Z_{eff} profile has been assumed in the simulations (an analysis of how sensitive model results are with respect to its value being left for section 4). Measurements of the total bulk radiation P_{rad} have been obtained for all three discharges using the vertical bolometer camera, but reconstruction of profiles for the radiative power density Q_{rad} has only been possible before the current ramp-down phase, so Q_{rad} profiles have been reconstructed at $t = 55\text{s}$ and the same shape (duly normalized to P_{rad}) has been kept in time during simulations. Figure 2 depicts the time traces for the line-averaged Z_{eff} , the gas puffing rate G_{puff} (a particle source discussed in section 3) and the total radiated power P_{rad} , together with their respective linear (or piecewise linear) fits used as inputs for the simulations, whilst the initial profiles for n_e , T_e , the safety factor q (as provided by EFIT [34, 35]) and Q_{rad} are given in figure 3.

3. MODELLING FRAMEWORK

3.1. L-MODE BgB MODEL.

In essence, the L-mode BgB model is an empirical transport model in which the electron and ion thermal diffusivities (ϵ_e and ϵ_i , respectively) are sums of Bohm-like and gyro-Bohm-like terms, each multiplied by a coefficient suitably tuned with recourse to a large profile database assembled from different tokamak experiments [1]. The BgB model equations are thus [1, 2, 3, 4, 5]:

$$\begin{aligned}\chi_{e,i} &= \chi_{B-e,i} + \chi_{gB-e,i}, \\ \chi_{B-i} &= 2 \chi_{B-e}, \\ \chi_{gB-i} &= 0.5 \chi_{gB-e}, \\ \chi_{B-e} &= 2 \times 10^{-4} \frac{a_0}{B_0} \frac{q^2}{n_e} \left| \frac{\partial (n_e T_e)}{\partial \rho} \right|, \\ \chi_{gB-e} &= 5 \times 10^{-6} \frac{\sqrt{T_e}}{B_0^2} \frac{\partial T_e}{\partial \rho}\end{aligned}$$

and

$$D = S \frac{\chi_e \chi_i}{\chi_e + \chi_i},$$

where D is the particle diffusivity (with S a weighting function decreasing linearly with the flux coordinate ρ from $S = 1.0$ on axis to $S = 0.3$ at the edge), $a_0 = (R_{\text{out}} - R_{\text{in}})/2$ (with R_{out} and R_{in} the outer and inner major radii of the last closed magnetic surface, respectively), B_0 is the magnetic field on axis, q , n_e and T_e are the local values of the safety factor and of the electron density and temperature, respectively, $\rho = \sqrt{\Phi/\pi B_{\text{ref}}}$ (with Φ the toroidal magnetic flux and B_{ref} the vacuum magnetic field at some reference geometrical centre, typically at $R_{\text{ref}} = 2.96\text{m}$ in JET)¹, and all quantities are in SI units but for T_e , which is in eV.

3.2 EQUILIBRIUM, CURRENT DIFFUSION AND SAWTOOTH MODEL.

Plasma equilibrium has been self consistently recalculated internally in JETTO every 45 ms with the xed-boundary ESCO solver, the separatrix being imported from EFIT, the reference vacuum magnetic field B_{ref} varying as in figure 1. For sawteeth, and prescribing a minimum crash period of 0.1 s, Kadomtsev's sawtooth mixing model has been used [36, 37] which, after a sawtooth crash, modifies the safety-factor, density and temperature profiles inside the mixing radius (defined by the flux surface that reconnects with the magnetic axis of the pre-crash configuration). Conservation of particles and energy combine with Kadomtsev's helical- flux-mixing algorithm to re-distribute particles and energy in such a way that they follow the reconnection of magnetic flux surfaces, which determines the instantaneous temperature and density reductions during the crash. Basically, flux surfaces with the same helical flux are reconnected inside the mixing region whilst conserving the toroidal flux, the net effect being generally to flatten plasma profiles. In particular, the q values are increased inside the $q = 1$ surface and reduced outside (between the $q = 1$ and the mixing radii), the post-crash q profile having $q = 1$ on axis. It will be shown in section 4 that the inclusion of a sawtooth model in the simulations is crucial to ensure agreement with experiments. In-between sawtooth crashes the evolution of the q profile is simulated using the current diffusion equation, the neoclassical resistivity and bootstrap current being computed by the NCLASS module implemented in JETTO [38], the evolution of temperatures and density being simulated using the energy and particle transport equations.

3.3. TRANSPORT CALCULATION AND SOURCES.

The set of plasma transport equations is solved in JETTO including both anomalous and neoclassical transport, the former given by the above L-mode BgB diffusivities and the latter provided through the NCLASS module (also used in the diffusion equation for the current density j) [38], thus yielding the profiles for n_i (with n_e obtained from the quasi-neutrality condition), T_e , T_i and j as functions of the flux coordinate ρ . The boundary condition for the j equation is the total plasma current I_p , depicted in figure 1, whereas for temperatures boundary conditions have been taken constant in time and the same for both ions and electrons, and for all three shots, namely, $T_{eb} = T_{ib} = 100\text{eV}$. Regarding density boundary conditions, they have been given for ions in the form of time polygons (whose vertices are joined via straight lines) according to: for Pulse No: 75225, $n_{ib} = 0.4 \times 10^{19} \text{ m}^{-3}$ between

¹Whenever profiles are plotted as functions of ρ , the latter coordinate is renormalized to its value at the plasma boundary.

$t = 15\text{s}$ and $t = 17\text{s}$, $n_{ib} = 0.3 \times 10^{19} \text{ m}^{-3}$ between $t = 18\text{s}$ and $t = 19\text{s}$, $n_{ib} = 0.2 \times 10^{19} \text{ m}^{-3}$ between $t = 20\text{s}$ and $t = 23\text{s}$, and $n_{ib} = 0.1 \times 10^{19} \text{ m}^{-3}$ for $t = 24\text{s}$; for shot Pulse No:76793, $n_{ib} = 0.2 \times 10^{19} \text{ m}^{-3}$ for $t = 15\text{s}$ and $n_{ib} = 0.1 \times 10^{19} \text{ m}^{-3}$ for $t = 24\text{s}$; for Pulse No:77922, $n_{ib} = 1.0 \times 10^{19} \text{ m}^{-3}$ for $t = 15\text{s}$ and $n_{ib} = 0.3 \times 10^{19} \text{ m}^{-3}$ between $t = 15.03\text{s}$ and $t = 24\text{s}$. Various heat sources and sinks enter the equations for T_e and T_i , the ones computed being OH heating, electron-ion collisional energy exchange and, for the ion energy balance, CX losses, whereas radiative losses in the electron energy balance are taken as measured with the levels and profiles given in figures 2 and 3. There are two particle sources in the equation for n_i , gas puffing and recycling, an average energy of $E_{neut} = 300\text{eV}$ being allowed in JETTO for all incoming neutrals (a rationale for its choice being postponed to section 4), which neutrals are modelled with recourse to FRANTIC (called every 50 time steps) [39]. The present simulations concern only the plasma conned inside the separatrix, so gas puffing and recycling are particle sources that must be understood here to be taken at this boundary (the first giving the rate at which fresh particles are fed into the modelled plasma domain, the second the fraction of outgoing particles that are re-injected into it). Strictly speaking, the actual recycling coefficient R_{cyc}^w is a physical quantity defined at the machine wall (as the ratio between the particle fluxes from and into the latter) and usually close to unity, which differs from a recycling at the separatrix R_{cyc}^s because of the so-called fuelling efficiency f (the fraction of neutrals starting at the wall that reach the conned plasma within the separatrix), whence $R_{cyc}^s \approx f R_{cyc}^w$ (assuming all the ion out flux at the separatrix reaches the wall) [40].

3.4 BENCHMARKING METHODOLOGY.

In what follows, the gas puffing rate G_{puff} is taken as measured, and as shown in figure 2, whereas the recycling coefficient R_{cyc} in the model (which gives the fraction of the outgoing ion flux across the separatrix that is returned as neutrals) is adjusted to x the average electron density and temperature levels given by JETTO so that they follow in time the experimental traces as best as possible. Of course, the same tuning exercise could have been performed using a mix between R_{cyc} and G_{puff} (since both are particle source terms in the transport equations) but, stemming from a rationale of restraining as much as possible the freedom in choosing the input for the JETTO modelling, the choice has been made to use R as a single free parameter to fix the average electron density and temperature levels given by JETTO so that they follow in time the experimental traces as best as possible². In fact, whereas no reliable measurement of particle recycling is available, the rate at which particles enter the vacuum chamber through the gas valves is nonetheless known and given by G_{puff} . In any case, such has been essentially a modeller's option (deemed to be the best suited to minimize the arbitrariness in the choice of free parameters one is allowed to play with), and probably no great physical meaning should be attached to the absolute values of R_{cyc} and G_{puff} (except when the latter becomes nil before the end of the current ramp, as discussed later

²Both R_{cyc}^s and R_{cyc} designate recycling coefficients defined at the separatrix but they are not necessarily identical, since the former represents the actual physical quantity fR_{cyc}^w whilst the latter gives the value which is necessary to keep the modelled line-averaged density at its appropriate, experimental value and, as discussed later in section 4, only in some particular circumstances one has $R_{cyc} \approx R_{cyc}^s$.

in section 4), but rather to their relative value and variation (which have to be such as to reproduce the measured linear-averaged density).

4. MODELLING RESULTS AND DISCUSSION

4.1 MODEL PREDICTIONS VERSUS EXPERIMENTS.

The comparison between modelled and experimental time traces for l_i , \bar{n}_e and $\langle T_e \rangle$ is shown, for the three JET shots under analysis, in figures 4 to 6, where are also given the time traces for the particle sources G_{puff} (as measured) and R_{cyc} (as tuned). The first general conclusion to be drawn is that, by simply adjusting the recycling coefficient R_{cyc} , the BgB model is capable to follow quite well the time evolution of l_i , \bar{n}_e and $\langle T_e \rangle$, which are the average plasma parameters linked to the current (or poloidal magnetic field), density and temperature profiles, respectively. To check that good agreement is not limited to these integrated quantities, a comparison between modelled and experimental n_e and T_e profiles (as given by HRTS and its synthetic diagnostic counterpart in JETTO) is presented in figures 7 to 12 as well.

4.2 QUANTITATIVE ERROR ANALYSIS.

To better quantify the agreement between model and experimental results (identified below by mod and exp, respectively), time-average and overall profile relative errors have been defined and computed according to [41]³.

$$\begin{aligned} \epsilon_Y &= \frac{1}{\Delta t} \int_t^{t+\Delta t} dt \frac{|Y_{\text{mod}}(t) - Y_{\text{exp}}(t)|}{Y_{\text{exp}}(t)} \\ &\approx \frac{1}{N} \sum_{n=1}^N \frac{|Y_{\text{mod}}(t_n) - Y_{\text{exp}}(t_n)|}{Y_{\text{exp}}(t_n)} \end{aligned}$$

and

$$\begin{aligned} \epsilon_X(t) &= \frac{\int_{R_{\min}}^{R_{\max}} dR |X_{\text{mod}}(R, t) - X_{\text{exp}}(R, t)|}{\int_{R_{\min}}^{R_{\max}} dR X_{\text{exp}}(R, t)} \equiv \frac{\int_{R_{\min}}^{R_{\max}} dR \Delta X(R, t)}{\int_{R_{\min}}^{R_{\max}} dR X_{\text{exp}}(R, t)} \\ &\approx \frac{\sum_{m=1}^{M-1} [\Delta X(R_{m+1}, t) + \Delta X(R_m, t)](R_{m+1} - R_m)}{\sum_{m=1}^{M-1} [X_{\text{exp}}(R_{m+1}, t) + X_{\text{exp}}(R_m, t)](R_{m+1} - R_m)}, \end{aligned}$$

where $Y(t)$ designates the time-evolving plasma parameter Y (which can be here l_i , \bar{n}_e or $\langle T_e \rangle$) and $X(R, t)$ the time-evolving profile of the quantity X (which represents here either n_e or T_e). Moreover, Δt is the time spanned by the traces in figures 4 to 6, R_{\min} and R_{\max} denote the interval spread over major radius by the profiles in figures 7 to 12, N is the number of experimental time samples (which needs not be the same for the different Y 's), and M the number of experimental radial points (which are not equally spaced in R)⁴. The relative errors defined above are given in table 1 for the global

³J.P.S. Bizarro appears as J.P. Bizarro in some earlier papers [41].

⁴The predicted $Y_{\text{mod}}(t_n)$'s and $X_{\text{mod}}(R_m, t)$'s, taken at the same t_n 's and R_m 's as the measured $Y_{\text{exp}}(t_n)$'s and $X_{\text{exp}}(R_m, t)$'s, have been obtained via interpolation of the simulation results, with the additional conditions $X_{\text{mod}}(R_{\min}, t) = X_{\text{mod}}(R_1, t)$ and $X_{\text{mod}}(R_{\max}, t) = X_{\text{mod}}(R_M, t) = 0$.

plasma quantities I_i , n_e and $\langle T_e \rangle$, and in table 2 for the n_e and T_e profiles. If one excludes the last second or so of the current ramps, already at very low plasma current (and well within the soft-stop phase of the discharge mentioned in section 2), when measurements may become less reliable and measured values quite small (as can be checked in figures 9 and 10 to be particularly true for Pulse No: 76793 and explaining its abnormally high values of n_e and T_e at $t = 24\text{s}$ shown in table 1), only very few relative errors are significantly above 20% which, as far as tokamak transport modelling is concerned, can be seen as indicating good agreement between model predictions and experiments.

4.2 RESPONSIVENESS TO R_{cyc} AND MODEL BEHAVIOR.

To gauge the responsiveness of the model to variations in recycling and because, of all three shots, Pulse No:75225 is the one showing the poorest agreement between the predicted and measured $\langle T_e \rangle$, a better t to the latter has been sought by retuning R_{cyc} (thus yielding the green curves instead of the blue ones in figures 4, 7 and 8). One sees that improving the t to $\langle T_e \rangle$ is indeed possible (with also a slight improvement in the t to I_i), but at the expenses of visibly worsening the agreement between model and experimental data for n_e . In fact, one of the features that has been recurrent in the present simulations using the BgB model is this trade-off that emerges when trying to refine the agreement in electron density and temperature: if both time traces n_e and $\langle T_e \rangle$ are not simultaneously reproduced satisfactorily by tuning particle recycling (as has been the case with Pulse No:75225), any attempt to better the agreement in one of them always implies degrading the agreement in the other. More precisely, whenever one goes up, the other comes down as if the product between these two quantities were to remain roughly constant. Indeed, OH plasmas are characterized by a strong coupling between the time evolutions of electron temperature, density and current density. Temperature and current strongly affect each other via the j dependent Joule's heating and the T_e dependent resistivity, a coupling that is further enhanced in the BgB model by the q^2 dependence of the Bohm contribution χ_{B-e} to thermal diffusivity. Moreover, when density is evolved self-consistently with temperature and current, variations in n_e affect T_e , not only due to the power balance equation, but also because of the χ_{B-e} dependence on the density and its gradient. So, when in figure 4 the density increases because of a stronger recycling, the electron temperature would reduce if the total heating power P_{heat} to electrons were kept fixed (for instance, by means of auxiliary heating) and the plasma were in a quasi-steady state since, in such a case, $(d/dt) \int n_e T_e dV \approx 0$ and power balance would yield $P_{heat} \approx \int n_e T_e dV / \tau$ (the integrals being over the plasma volume V and τ being the confinement time). However, in OH regimes the OH heating power P_{OH} depends on T_e via resistivity, more precisely, the respective power density goes as $dP_{OH}/dV = jE_{||} \approx \eta_{Spitzer} j^2 \sim T_e^{-3/2} j^2$ (with $E_{||}$ the parallel electric field), so a reduction in T_e leads to a rise in resistivity and OH heating becomes more efficient (at fixed current density j), partly compensating for the T_e reduction. This explains why, in figures 4, 7 and 8, the decrease in temperature is less pronounced than the increase in density. As for the transport coefficients, the increase in n_e and therefore in its gradient tends to enhance BgB transport whereas the T_e reduction works the other way around by depleting

diffusivities and also particle diffusion. As a result, the transport coefficients are nearly the same at high and low recycling which implies, in conclusion, that the temperature response to a higher R_{cyc} is mainly determined by the non-linear coupling between n_e and T_e induced by OH heating rather than by transport. This analysis and conclusions have been corroborated by time-sampling profiles of electron density and temperature, plasma current density, electric field, OH-heating power density and electron thermal diffusivity for the two cases (blue and green) compared in figures 4, 7 and 8. An example for shot Pulse No:75225 at $t = 19s$ is shown in figure 13, where one can check that, when T_e comes down, n_e , E_\parallel and dP_{OH}/dV do go up, whereas j and e remain essentially unchanged.

4.3 SENSITIVENESS TO Z_{eff}

Considering that $n_e \approx n_i / [1 - (Z_{eff} - 1)/5]$ in a quasi-neutral Deuterium plasma with Carbon as main impurity, the influence of Z_{eff} has been assessed, in particular to see if, by readjusting its value within the experimental uncertainty, the behavior alluded to above can be circumvented. The simulations for shot Pulse No: 75225 have thence been repeated by varying Z_{eff} in $\pm 10\%$, the outcome being depicted in figure 14, which shows there is no significant impact on model results, the most noticeable effect being on I_i via the influence of Z_{eff} on plasma resistivity and, therefore, on current diffusion [24].

4.4 CHOICE OF E_{neut}

Assuming equipartition, note that the average energy of $E_{neut} = 300eV$ taken for neutrals entering the plasma through the separatrix corresponds to a temperature of $T_{neut} \approx 150eV$, slightly above the boundary value of $T_{ib} = 100eV$ taken for ions, which ensures adequate neutral penetration. Actually, and to be on the safe side, neutral energies E_{neut} of $50eV$ and $150eV$ have been used in trial checks for Pulse No:77922, the outcome being given in figure 15 and showing these values make it virtually impossible to reach the required density level (inasmuch as, according to figure 6, gas puffing is already switched off and recycling is already at its maximum value of one for a significant part of the current ramp).

4.5 IMPORTANCE OF SAWTOOTH MODEL.

It is also interesting to check how important it is to couple the BgB transport model to a sawtooth model, an assessment that has been conducted by switching off the latter and repeating the calculations for Pulse No: 77922. As shown in figure 16, there is a remarkable impact on I_i (concomitant with a less pronounced, but still significant, effect on $\langle T_e \rangle$), which indicates that the current diffusion calculation has completely changed and demonstrates how crucial the role of the sawtooth model is in ensuring correct reproduction of the experiments (in which, it is worth recalling, sawteeth have indeed been observed). Note that simply retuning R_{cyc} wouldn't do because, to lower the predicted I_i and $\langle T_e \rangle$ in figure 16, one would necessarily have to increase n_e (according to the discussion on model behaviour in a previous paragraph) and R_{cyc} is already unity (or very close to it) for most of

the current ramp (as can be checked in figure 6), precisely when the difference between the modelled l_i 's becomes larger and larger. To go into more detail, profiles at two different instants (before and during the ramp) are compared (with and without sawtooth model) in figure 15 for n_e , T_e , q and the flux-surface averaged poloidal field B_{pol}^+ . When the sawtooth model is switched off, there is no longer a periodic redistribution of the q and T_e profiles whose basic outcome is to flatten them inside the mixing radius (here roughly at $\rho \approx 0.4$), whence a significant increase in B_{pol} and T_e in the inner plasma regions, which translates into a much larger $l_i \sim \langle B_{pol}^2 \rangle$ and also into higher $\|T_e\|$ values. Note that it is important for ITER to limit the excursion of l_i during the ramp-down phase to ensure vertical stability [30], which the simulation without sawteeth is not capable to ensure.

4.6. PHYSICAL MEANINGFULNESS OF R_{cyc} .

The recycling coefficient R_{cyc} has played the key role in this benchmarking exercise for the BgB model in JETTO since, as explained in section 3, it has been the only tuning variable allowed. Now, the question may arise whether the values thus retrieved for R_{cyc} have any physical meaning or no, as the same match between predicted and measured quantities could eventually have been obtained by a different combination of R_{cyc} and G_{puff} , particularly considering that these two parameters vary almost in perfect opposition (as is apparent from figures 4 to 6). Nonetheless, in the final part of the current ramps G_{puff} becomes zero, which leaves R_{cyc} as the only source term in the particle transport equation and thus as the only means to control the plasma density, not only in the model but in the experiment as well. When this happens, it is highly plausible that the tuned R_{cyc} become very close to the actual recycling at the separatrix R_{cyc}^s , which allows one to infer that in the end of the ramps the true recycling coefficient at the wall R_{cyc}^w is indeed close to unity (summing up, recall that $R_{cyc}^s \approx fR_{cyc}^w$ while simultaneously, in this part of the discharge, $R_{cyc} \approx 1$ and $R_{cyc} \approx R_{cyc}^s$) [40]. Interestingly enough, such an inference (in essence, that the fuelling efficiency increases and becomes close to one, $f < 1$) is consistent with the experimental fact that the plasma is indeed displaced towards the machine wall in the final stages of these discharges, as illustrated in figure 18 for Pulse No: 75225, where it is clear that the plasma boundary touching the wall is much larger at $t = 23.5s$ than at $t = 15.0s$. However, note there may be an alternative explanation for having $fR_{cyc}^w \approx 1$ at the end of the ramps: that the wall may be loosing particles simply because it is heating up due to increasing plasma proximity, which would correspond to a situation where $R_{cyc}^w \geq 1$ whilst keeping $f < 1$. Thus, although the type of modelling performed here (which concerns plasma transport inside the separatrix) may allow some conjectures to be drawn about recycling and fuelling, it must be kept in mind that it cannot provide a definite answer to the complex interplay between the wall reservoir, recycling, transport in the scrape-off layer and fuelling efficiency.

5. SUMMARY AND CONCLUSIONS

This paper reports on the use of the L-mode version of the BgB model in JETTO to fully predict

⁵The B_{pol} profiles in figure 17 do not come directly from the equilibrium but from Faraday's equation, and so account for poloidal-field diffusion between calls to the equilibrium solver.

transport (more precisely, the profiles for current and plasma densities and for ion and electron temperatures) during the current ramp-down phase of JET hybrid discharges. A good agreement between model and experiments has been obtained by tuning the particle sources in such a manner as to follow as best as possible the measured time traces for the linear-average density and volume-average temperature. A quantitative error analysis conducted on the deviations between model and experimental time traces for internal inductance, linear-average density and volume average temperature as well as for profiles of electron density and temperature yields relative errors falling mostly below 20%. Of the two available particle sources entering the model, namely, gas puffing and recycling (considered here at the separatrix), the option has been made to take for the former the actual rate at which gas is injected into the vacuum vessel and to vary the latter (for which no trustable experimental value truly exists) so as to keep the plasma density at the appropriate level. JETTO solves for plasma transport inside the separatrix, so the rate at which, in the model, neutrals are fed into the core plasma through the latter is not necessarily identical to the actual rate at which gas is puffed into the vessel (what happens in the scrape off layer is not accounted for in the modelling), implying that recycling (the fraction of outgoing ions through the separatrix that are returned as neutrals) in the model may not be the same as in the experiment (without mentioning its difference to the actual recycling at the machine wall). Even so, in the final stages of the discharges (when gas puffing is switched off) the model recycling coefficient (tuned to follow the experimental linear-average density) eventually becomes close to the real recycling at the separatrix because it is the only particle source, both in experiments and in the simulations. It is then possible to infer from the modelling that the product between the wall recycling and the fuelling efficiency (which product defines the recycling at the separatrix) approaches one at the end of the current ramps, a possible indication that fuelling efficiency also becomes close to one (if roughly unit wall recycling is assumed), which is moreover consistent with the fact that the plasma does become into contact with the vessel's inner wall at this stage.

A feature found in the modelling has been the strong non-linear coupling between electron density and temperature: any attempt to make the model yield a better agreement with the experimental data for one of these quantities (by retuning the recycling coefficient) demands a trade-off on the agreement for the other, the two varying in opposition. Basically, this behaviour is present when trying to maintain quasi steady-state power balance with an approximately constant heating power (in which case an increase in electron density brings about a decrease in electron temperature and vice-versa), but a finer analysis brings to the front the intricate couplings that exist in the BgB model of a OH plasma between current density and electron temperature (via Joule's heating with a temperature-dependent resistivity and a Bohmlike thermal diffusivity depending on the safety factor), and between electron density and temperature (through the dependence on the respective gradients of the BgB transport coefficients). Because the effects arising from the variation in the density and temperature gradients in the BgB diffusivities tend to cancel each other (when density and temperature change in opposite manner), the Spitzer-like dependence of plasma resistivity on

temperature (the former increasing when the latter decreases, thus enhancing Joule's heating when expressed in terms of the current density instead of the electric field) explains why, in the end, changes in electron temperature are less pronounced than in density. This stiffness in the product between electron density and temperature (hence also in plasma pressure and energy density) manifested by BgB transport in a OH plasma has two strong consequences: if model predictions are well tuned to experimental results both in density and in temperature, the corresponding agreement is robust; otherwise, and all other things kept constant, there must be a trade off as a better match between model and experiments for one of the two quantities will generally imply a poorer agreement for the other. The sensitiveness of the modelling with respect to the ion effective charge has also been evaluated, having been found that varying this parameter within 10% (always keeping a constant profile across flux surfaces) has no significant impact on the simulation results. Assessed as well has been the choice of the value for the average energy of neutrals entering the plasma across the separatrix (either from gas puffing or recycling), a value of 300eV having been found to ensure penetration consistent with the experimentally verified density level. In addition, the importance of incorporating an appropriate sawtooth model (as Kadomtsev's used here) in the simulations has been shown; without it, model predictions could not be made to properly fit the experiments.

CONCLUSION

The usefulness of the BgB model as a predictive modelling tool for plasma transport in tokamaks has been reinforced by showing its robustness in reproducing, within acceptable uncertainty, the data measured during the OH current-ramp-down phase of JET pulses for different experimental conditions (different ramp rates, plasma densities and reference magnetic fields). Although lacking the appeal that first-principles models always have, empirical models such as BgB (easy to use and fast in running) remain nonetheless the workhorse of tokamak transport modelling, whilst benchmarking exercises as the one reported here continue to be important in well characterizing their domains of validity and in clearly identifying both their weaknesses and their strengths.

ACKNOWLEDGMENTS

Discussions with, and suggestions by, Paula Belo, Gerard Corrigan, Jorge Ferreira and Luca Garzotti are gratefully acknowledged. It is also a pleasure to thank Jörg Hobirk for many insightful comments, particularly in helping to clarify the discussion about the recycling coefficient and fuelling efficiency. This work has been conducted under the European Fusion Development Agreement (EFDA), its Task Force on Integrated Tokamak Modelling (TF-ITM) and, in particular within the latter, the EU-ITM ITER Scenario Modelling (ISM) Group, as well as within the frameworks of the Contract of Association between the European Atomic Energy Community and the Instituto Superior Técnico (IST) and of the contract of Laboratório Associado with the Fundação para a Ciência e a Tecnologia (FCT, Lisboa), under project no Pest-OE/SADG/LA0010/2011. The content of this paper is the sole responsibility of the authors and does not necessarily represent the views of the European Commission, of FCT, of IST, or of their services.

REFERENCES

- [1]. Erba M. et al 1997 Plasma Physics and Controlled Fusion **39** 261
- [2]. Parail V.V. et al 1999 Nuclear Fusion **39** 429
- [3]. Gohil P. et al 2003 Nuclear Fusion **43** 708
- [4]. Garzotti L. et al 2003 Nuclear Fusion **43** 1829
- [5]. Tala T. et al 2006 Nuclear Fusion **46** 548
- [6]. Litaudon X. et al 2007 Nuclear Fusion **47** 1285
- [7]. Krasheninnikov S.I. 2007 Nuclear Fusion **47** S529
- [8]. Bizarro J.P.S. et al 2007 Nuclear Fusion **47** L41
- [9]. Budny R.V. et al 2008 Nuclear Fusion **48** 075005
- [10]. Bizarro J.P.S. et al 2008 IEEE Transactions on Plasma Science **36** 1090
- [11]. Voitsekhovitch I. et al 2009 Nuclear Fusion **49** 055026
- [12]. Parail V.V. et al 2009 Nuclear Fusion **49** 075030
- [13]. Kessel C.E. et al 2009 Nuclear Fusion **49** 085034
- [14]. Kim S.H. et al 2009 Plasma Physics and Controlled Fusion **51** 105007
- [15]. Artaud J.F. et al 2010 Nuclear Fusion **50** 043001
- [16]. Coster D. et al 2010 IEEE Transactions on Plasma Science **38** 2085
- [17]. Voitsekhovitch I. et al 2010 Plasma Physics and Controlled Fusion **52** 105011
- [18]. Fable E. et al 2011 Nuclear Fusion **51** 043006
- [19]. Garcia J. et al 2011 Nuclear Fusion **51** 073019
- [20]. Imbeaux F. et al 2011 Nuclear Fusion **51** 083026
- [21]. Murakami M. et al 2011 Nuclear Fusion **51** 103006
- [22]. Garzotti L. et al 2012 Nuclear Fusion **52** 013002
- [23]. Citrin J. et al 2012 Plasma Physics and Controlled Fusion **54** 065008
- [24]. Fietz S. et al 2013 Nuclear Fusion **53** 053004
- [25]. Litaudon X. et al 2013 Nuclear Fusion **53** 073024
- [26]. Sips A.C.C. et al 2009 Nuclear Fusion **49** 085015
- [27]. Jackson G.L. et al 2009 Nuclear Fusion **49** 115027
- [28]. Politzer J.F. et al 2010 Nuclear Fusion **50** 035011
- [29]. Jackson G.L. et al 2010 Physics of Plasmas **17** 056116
- [30]. Sips A.C.C. et al 2010 Proc. 23rd IAEA Fusion Energy Conf. (Daejon, Republic of Korea, 2010) EXC/P2-08 http://www-naweb.iaea.org/napc/physics/FEC/FEC2010/papers/exc_p2-08.pdf
- [31]. Romanelli F. et al 2011 Nuclear Fusion **51** 094008
- [32]. Belo P. et al 2011 Proc. 38th EPS Conf. on Plasma Physics (Strasbourg, France, 2011) vol 35G (ECA) P1.119 <http://ocs.ciemat.es/EPS2011PAP/pdf/P1.119.pdf>
- [33]. Sartori F. et al 2009 Proc. 23rd IEEE/NPSS Symp. on Fusion Engineering (San Diego, CA, 2009) <http://dx.doi.org/10.1109/FUSION.2009.5226522>

- [34]. O'Brien D. P. et al 1992 Nuclear Fusion **32** 1351
- [35]. Brix M. et al 2008 Review of Scientific Instruments **79** 10F325
- [36]. Kadomtsev B. 1975 Soviet Journal of Plasma Physics **1** 389
- [37]. Porcelli F. et al 1996 Plasma Physics and Controlled Fusion **38** 2163
- [38]. Houlberg W.A. et al 1997 Physics of Plasmas **4** 3230
- [39]. Tamor S. 1981 Journal of Computational Physics **40** 104
- [40]. Ehrenberg J. 1996 First wall effects on particle recycling in tokamaks Physical Processes of the Interaction of Fusion Plasmas with Solids ed W. Off. Hofer and J. Roth (San Diego, CA: Academic) p. 35
- [41]. Bizarro J.P.S. and Moreau D. 1993 Physics of Fluids B **5** 1227

	#75225	#76793	#77922
ϵ_{l_i} (%)	2.2	3.1	3.3
$\epsilon_{\bar{n}_e}$ (%)	5.5	12.4	5.7
$\epsilon_{\langle T_e \rangle}$ (%)	20.9	20.3	8.2

Table 1: Time-average simulation errors in $l_i(t)$, $\bar{n}_e(t)$ and $\langle T_e \rangle(t)$ for Pulse No's: 75225, 76793 and 77922.

t (s)	ϵ_{n_e} (%)			ϵ_{T_e} (%)		
	#75225	#76793	#77922	#75225	#76793	#77922
15	7.6	10.8	9.0	19.0	17.7	12.9
16	14.7	20.8	9.0	16.7	16.1	13.6
17	16.3	21.0	11.1	14.5	21.4	10.8
18	11.5	19.6	9.8	25.7	12.5	15.0
19	11.9	15.3	8.5	26.6	16.5	18.4
20	16.5	17.5	11.6	22.5	18.2	16.0
21	13.1	15.0	13.4	22.3	13.8	16.5
22	14.5	14.9	11.9	20.8	25.9	12.8
23	15.1	31.0	15.6	33.0	31.7	19.8
24	20.8	86.0	21.6	27.2	138.3	20.7

Table 2. Overall profile simulation errors in $n_e(R; t)$ and $T_e(R; t)$, at different time slices, for Pulse No's: 75225, 76793 and 77922.

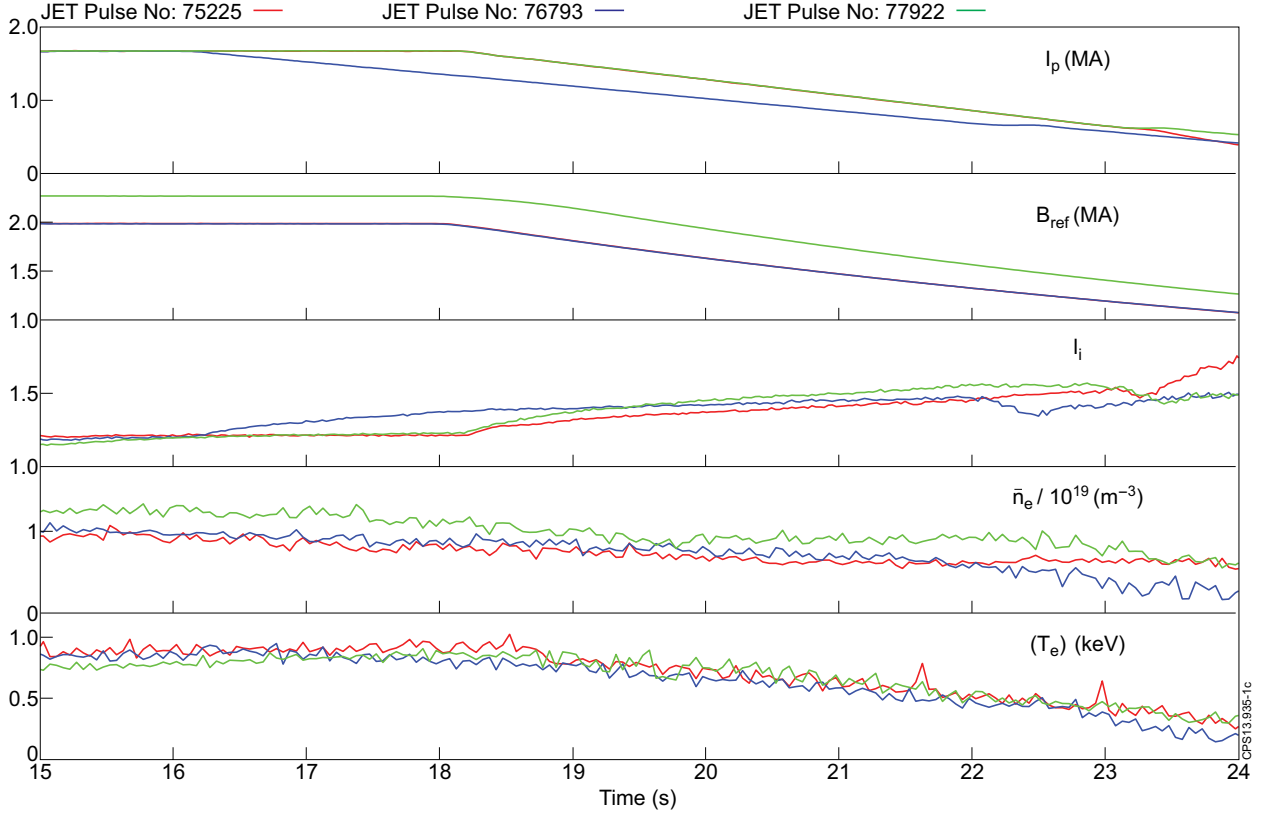


Figure 1: Experimental time traces for JET Pulse No's: 75225, 76793 and 77922: plasma current I_p , toroidal magnetic field B_{ref} , plasma internal inductance l_i , line averaged electron density n_e and volume-averaged electron temperature $\langle T_e \rangle$ versus time t .

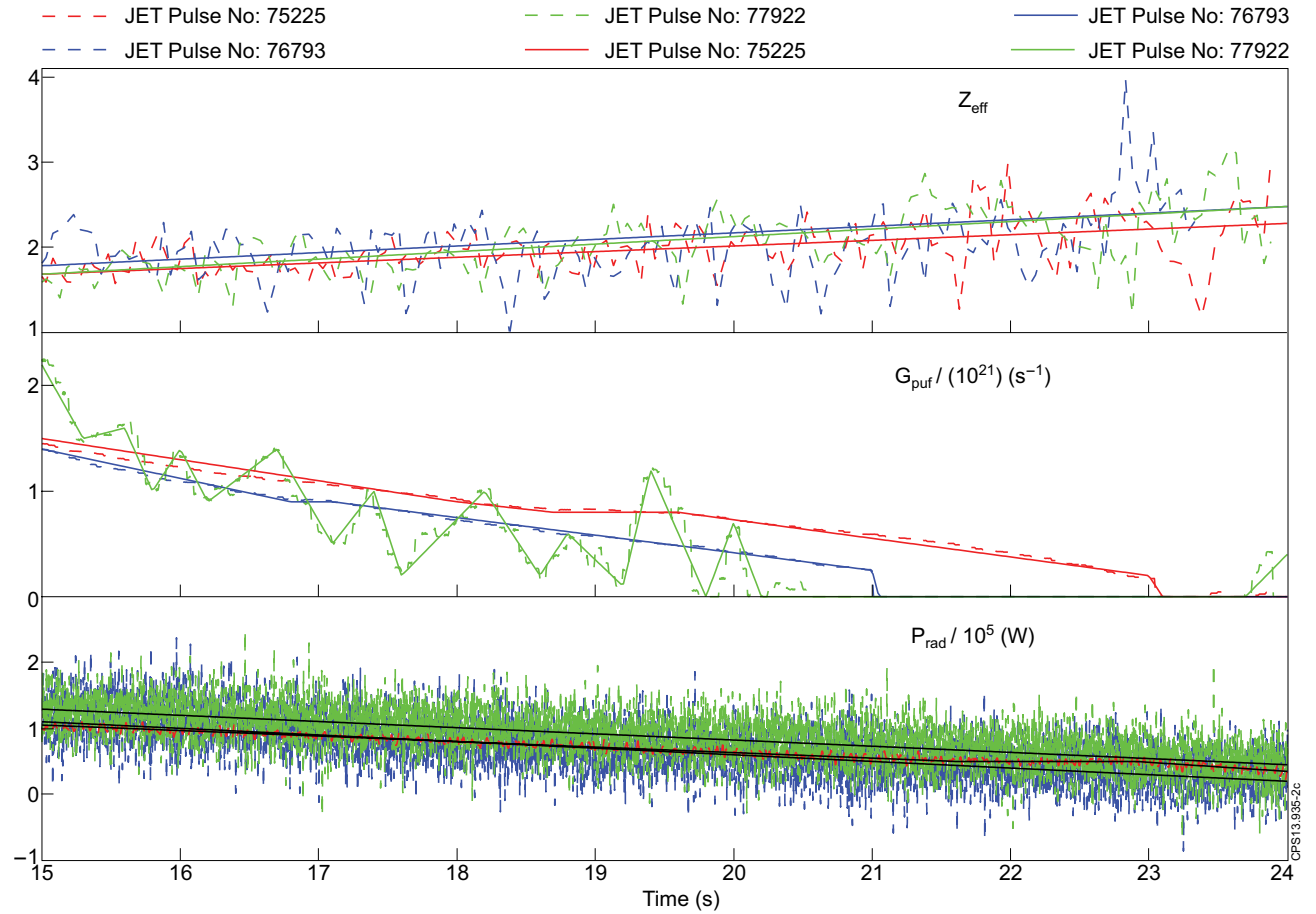


Figure 2: Experimental (dashed) and input (solid) time traces for JET Pulse No's: 75225, 76793 and 77922: ion effective charge Z_{eff} , gas puffing rate G_{puff} and total radiated power P_{rad} versus time t .

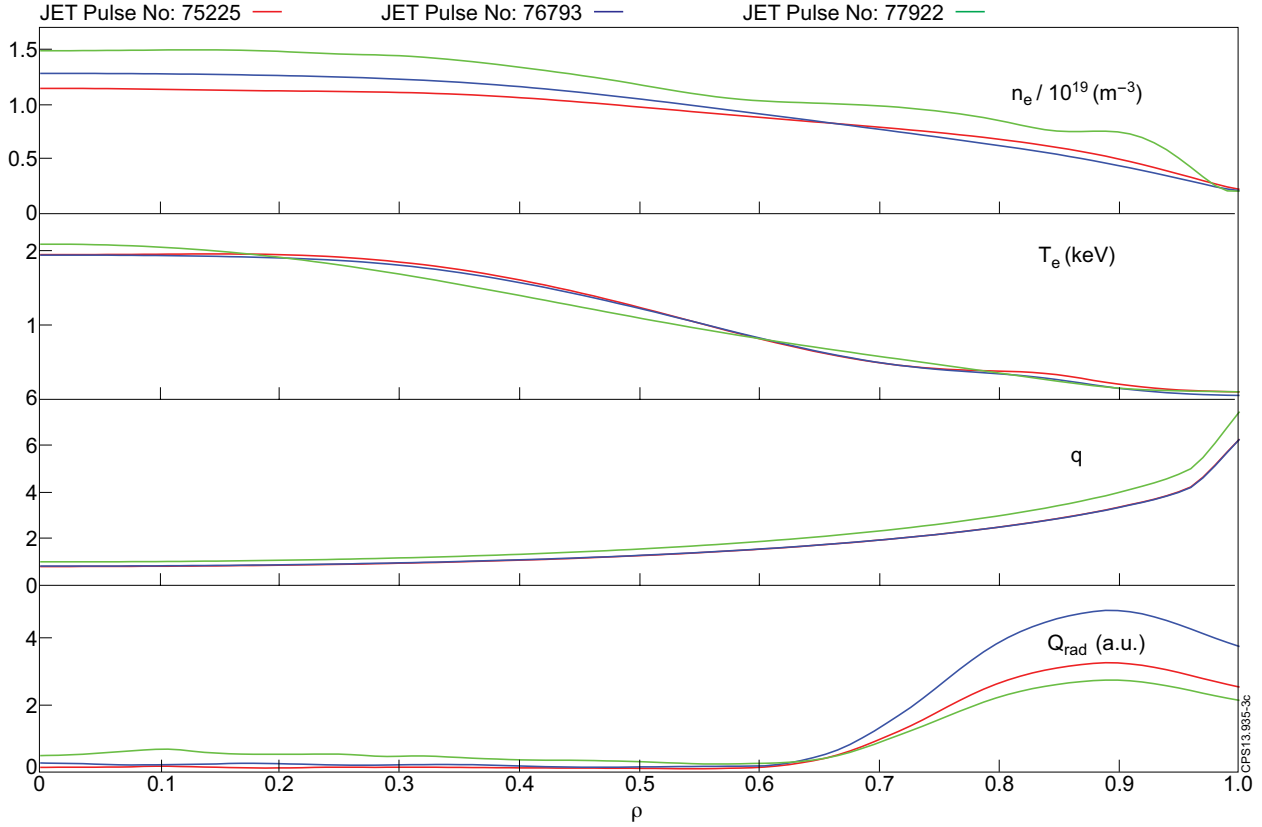


Figure 3: Input initial profiles for JET Pulse No's: 75225, 76793, and 77922: electron density n_e , electron temperature T_e , safety factor q and radiated power density Q_{rad} versus the flux coordinate ρ .

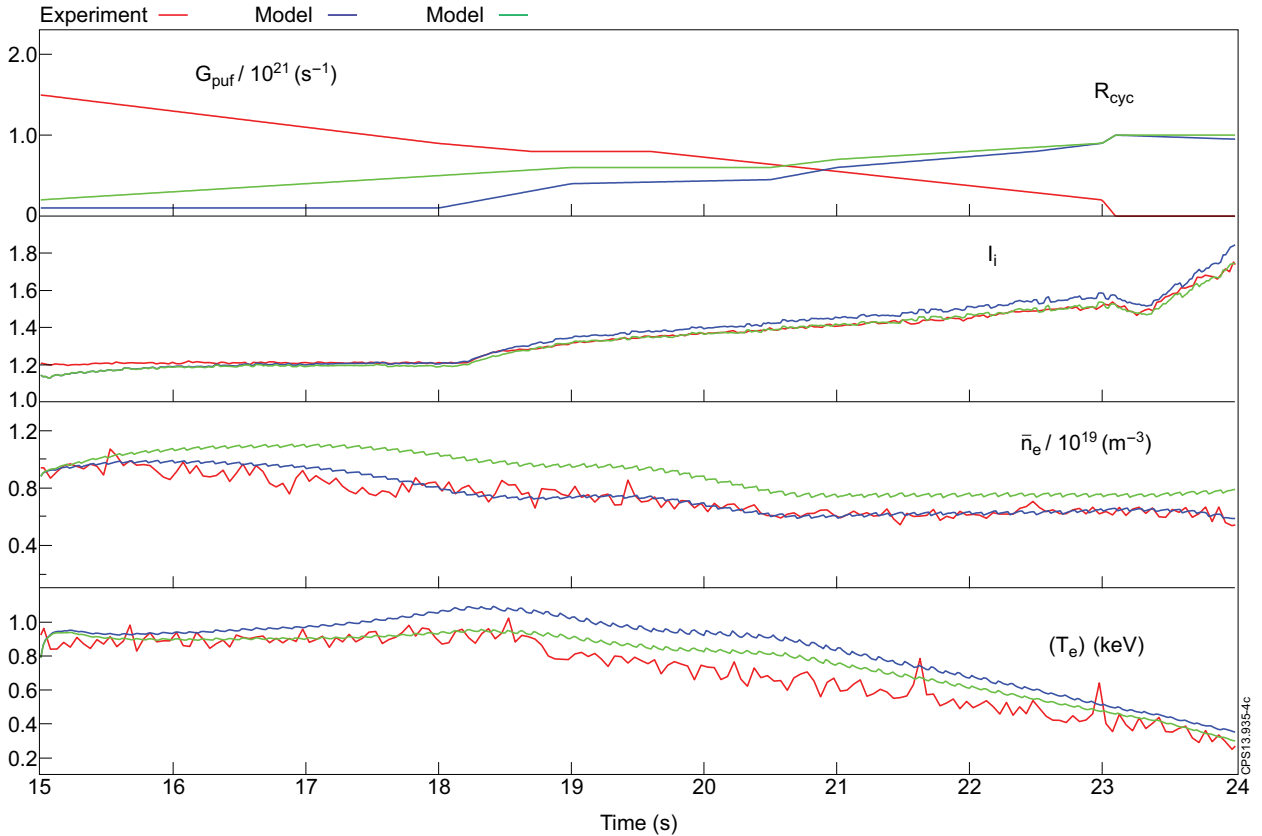
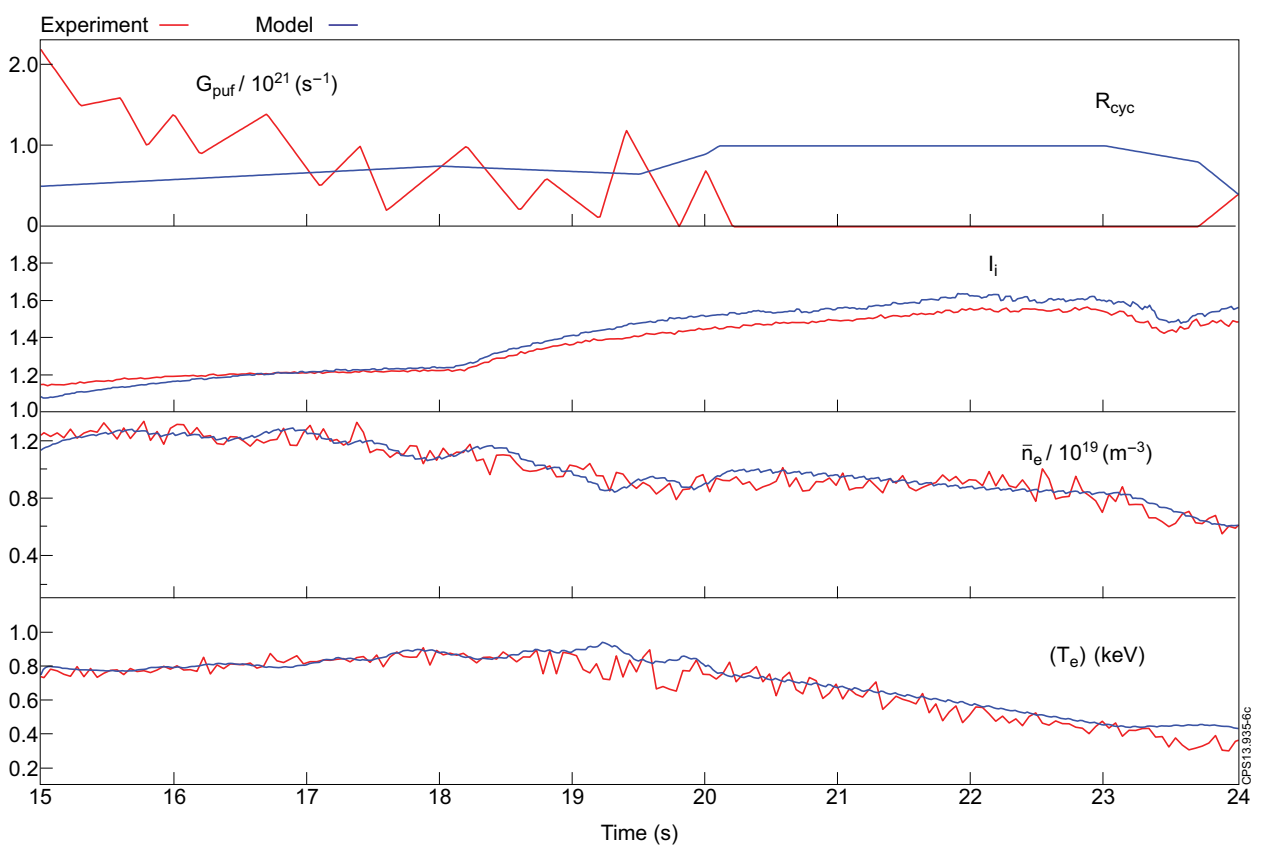
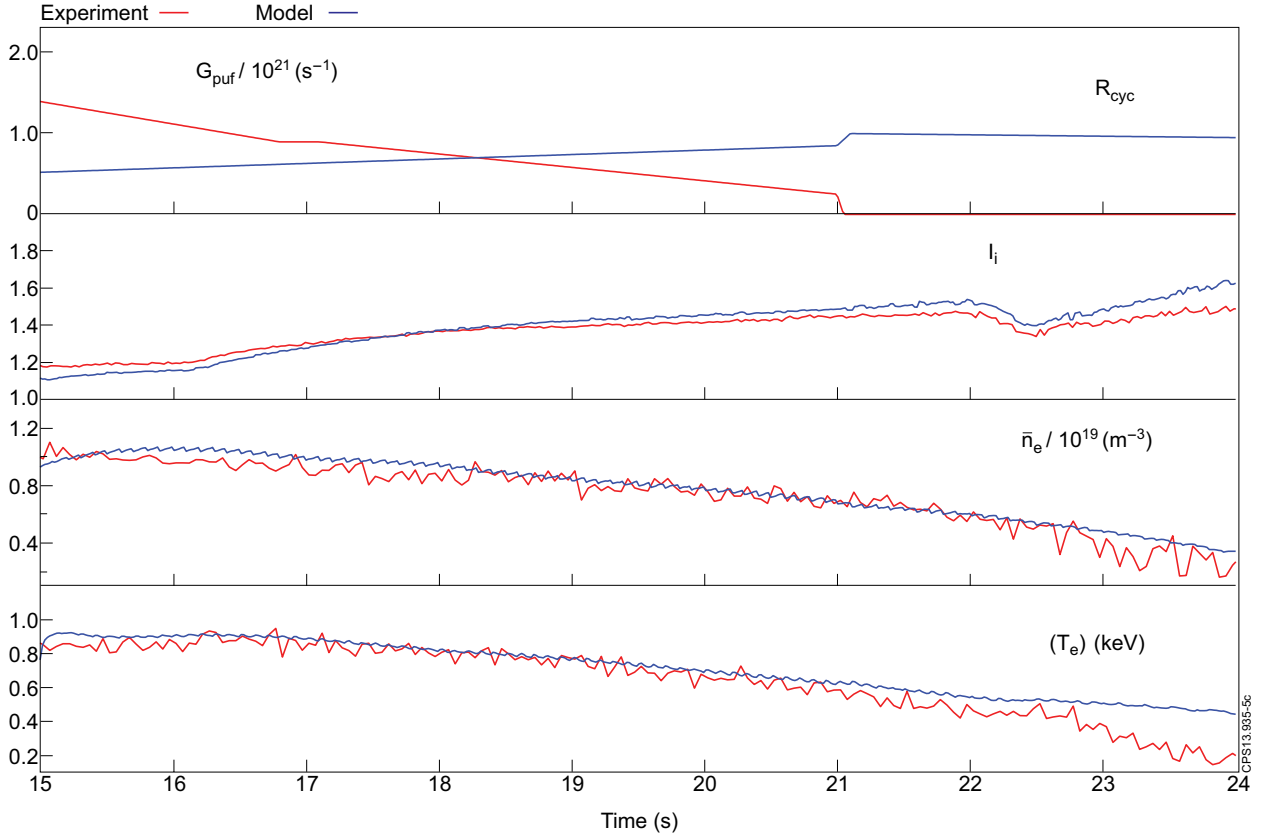


Figure 4: Model and experimental time traces for JET Pulse No: 75225: gas puffing rate G_{puff} , recycling coefficient R_{cyc} , plasma internal inductance l_i , line-averaged electron density n_e and volume-averaged electron temperature $\langle T_e \rangle$ versus time t .



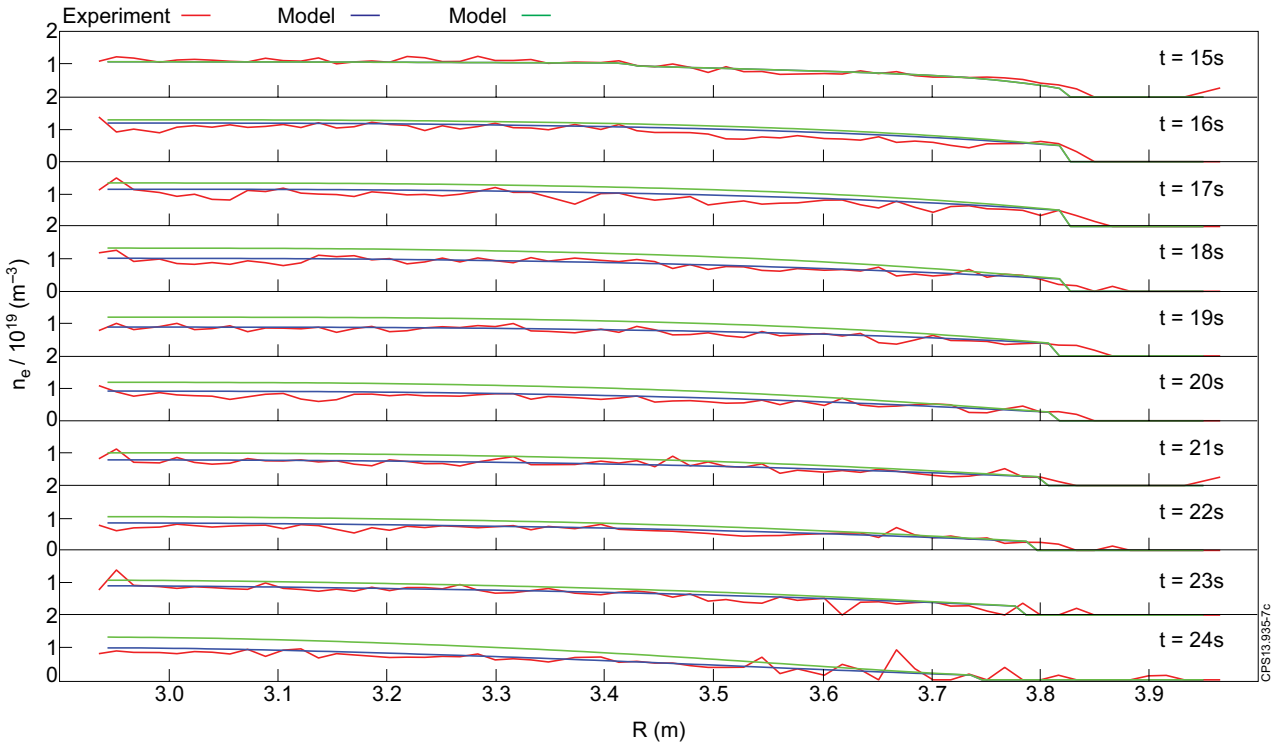


Figure 7: Model and experimental density profiles for JET Pulse No: 75225: electron density n_e versus major radius R for different times t .

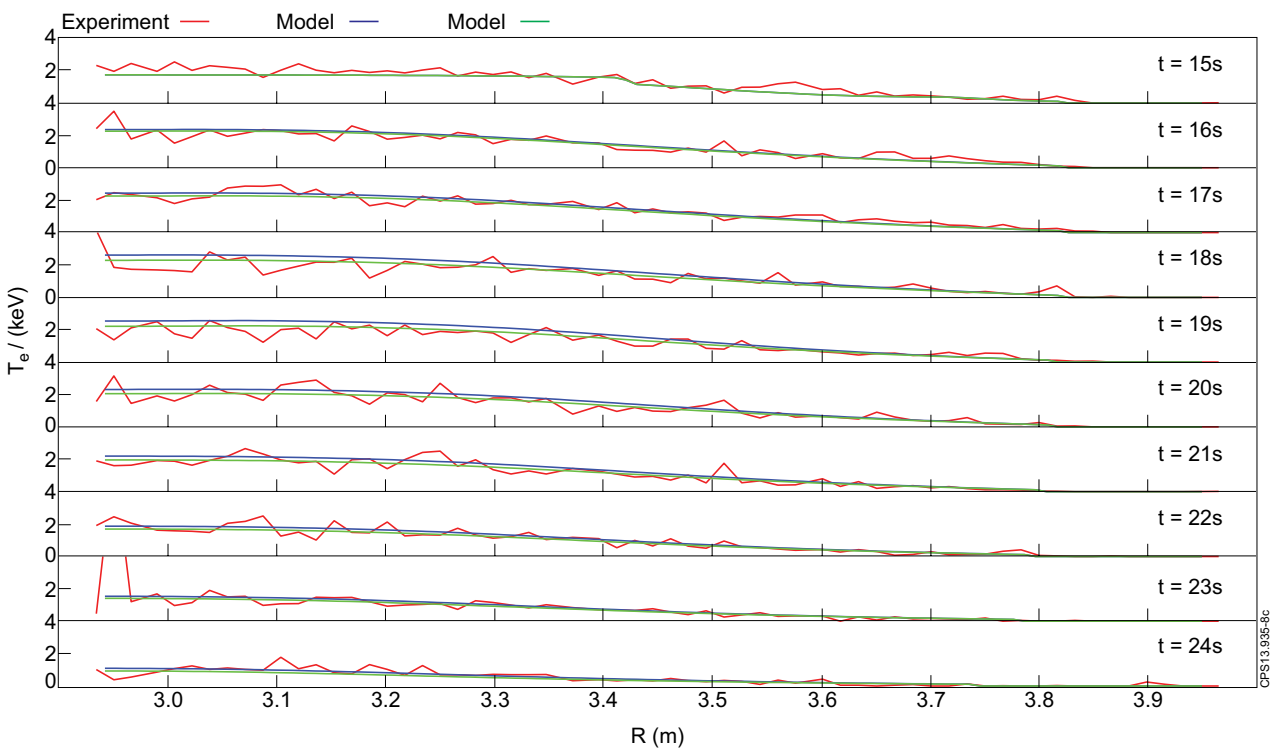


Figure 8: Model and experimental temperature profiles for JET Pulse No: 75225: electron temperature T_e versus major radius R for different times t .

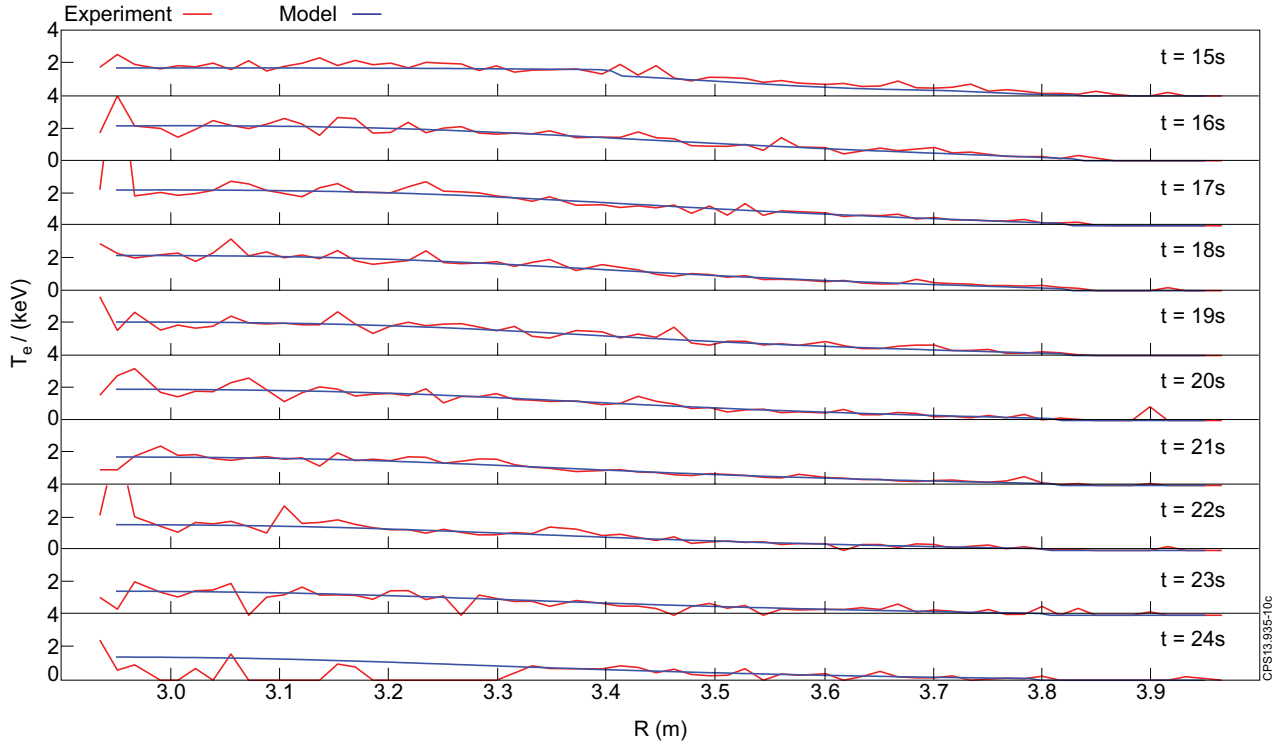


Figure 9: Model and experimental density profiles for JET Pulse No: 76793: electron density n_e versus major radius R for different times t .

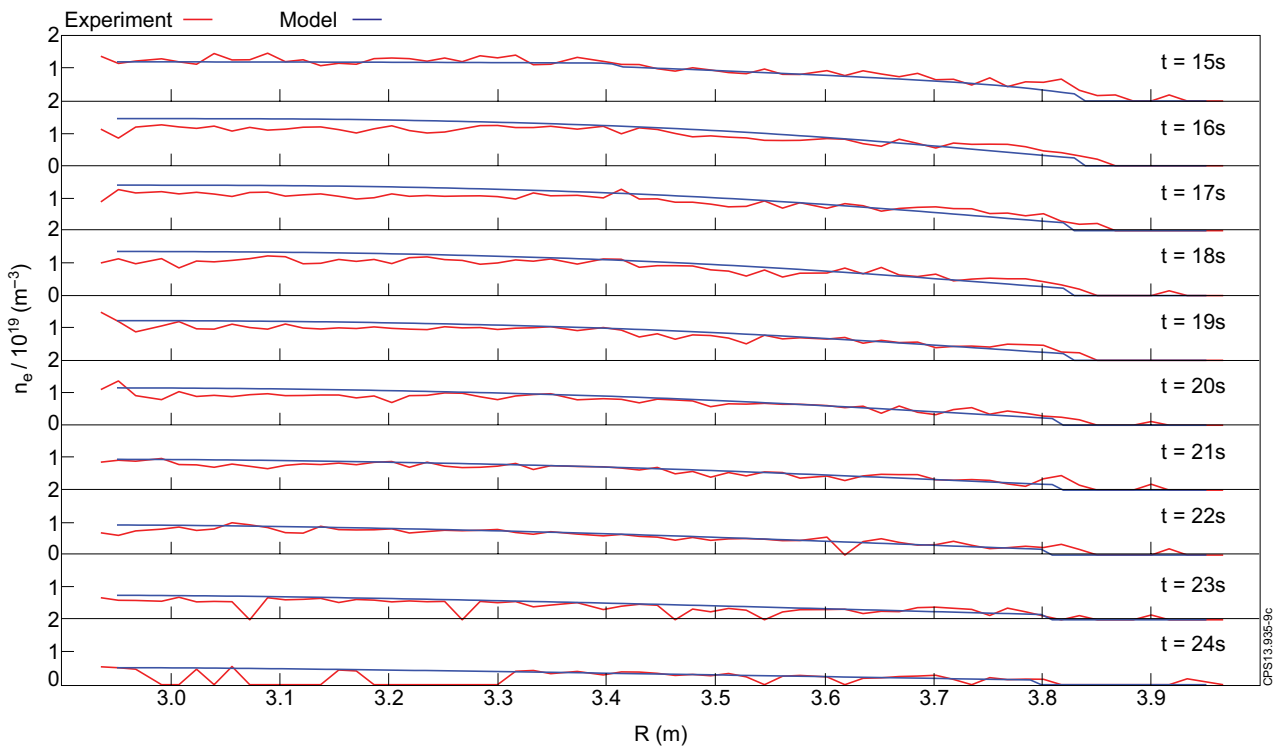


Figure 10: Model and experimental temperature profiles for JET Pulse No: 76793: electron temperature T_e versus major radius R for different times t .

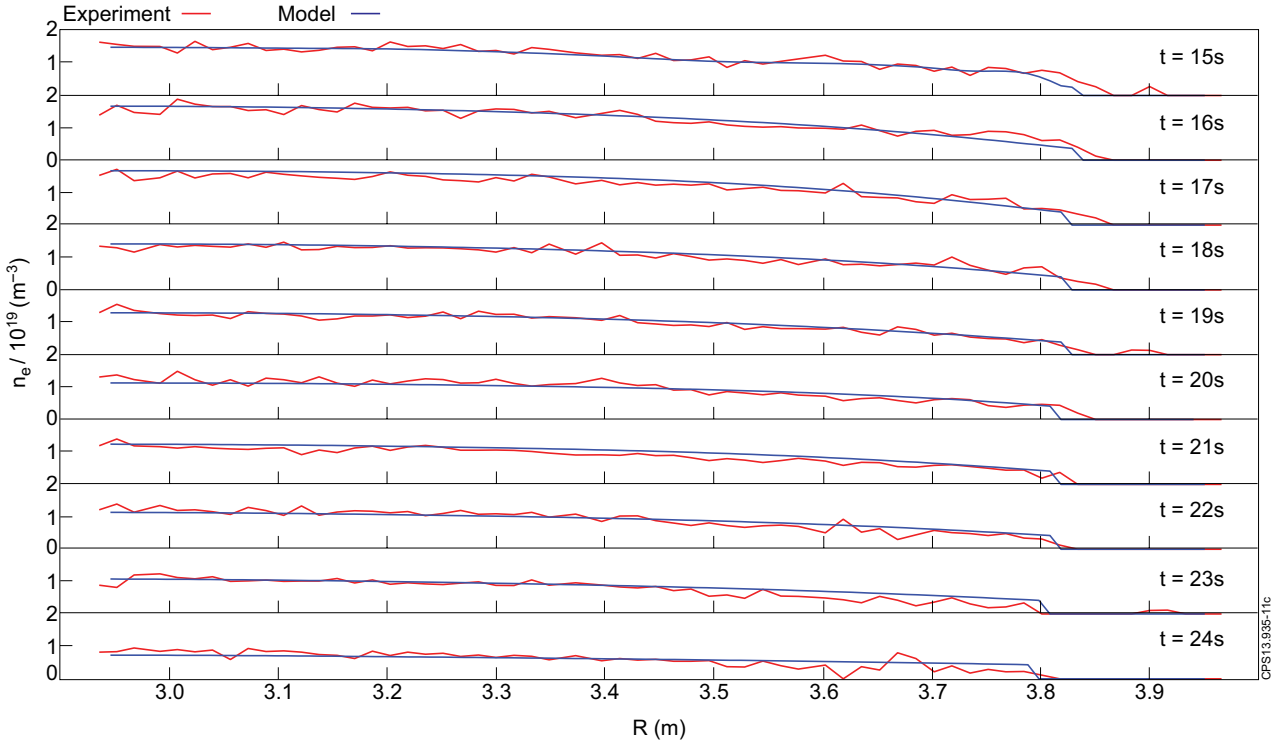


Figure 11: Model and experimental density profiles for JET Pulse No: 77922: electron density n_e versus major radius R for different times t .

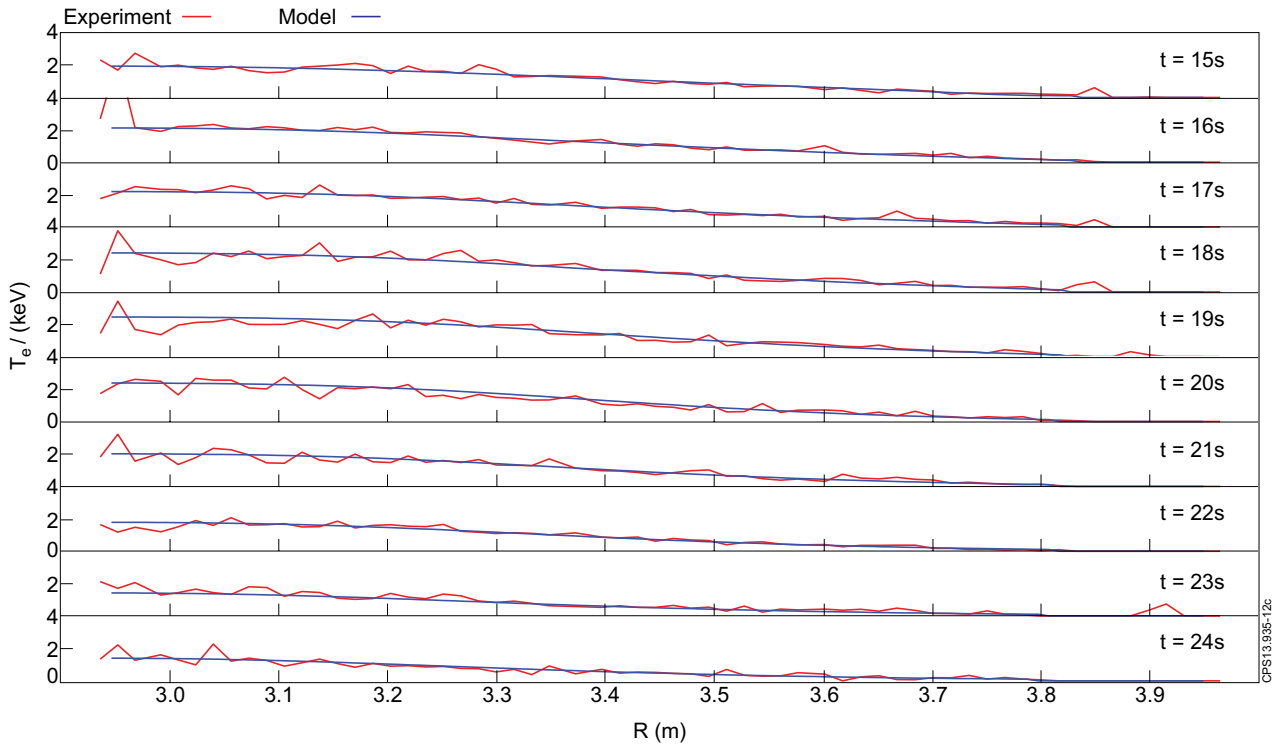


Figure 12: Model and experimental temperature profiles for JET Pulse No: 77922: electron temperature T_e versus major radius R for different times t .

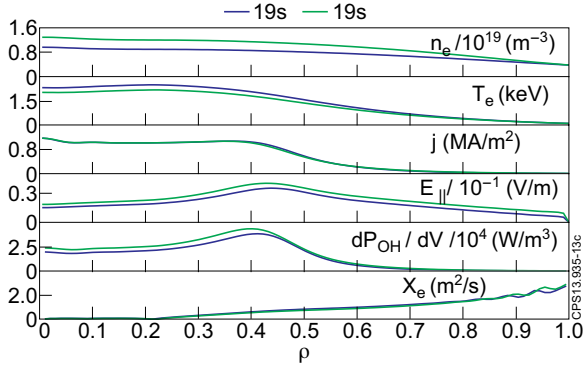


Figure 13: Model profiles for JET Pulse No: 75225 (comparing simulations during the current ramp, namely at $t = 19\text{s}$, for differently tuned recyclings): electron density n_e , electron temperature T_e , current density j , parallel electric field $E_{||}$, OH power density dP_{OH}/dV and electron thermal diffusivity χ_e versus flux coordinate ρ .

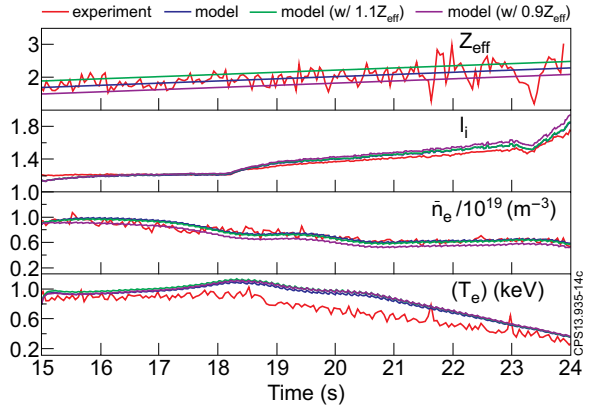


Figure 14: Model and experimental time traces for JET Pulse No: 75225 (comparing the reference model results with simulations with Z_{eff} varying within 10%): ion effective charge Z_{eff} , plasma internal inductance l_i , line-averaged electron density n_e and volume-averaged electron temperature $\langle T_e \rangle$ versus time t .

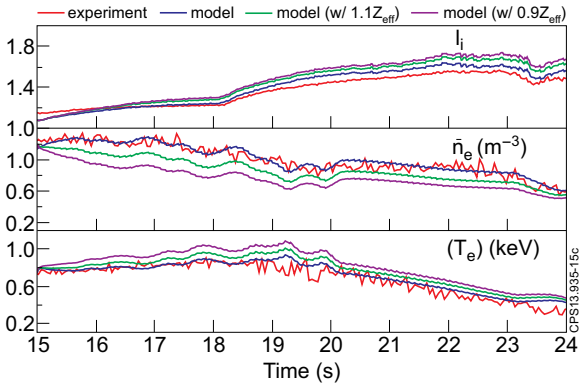


Figure 15: Model and experimental time traces for JET Pulse No: 77922 (comparing the reference model results with simulations with E_{neut} equal to 150eV and 50eV): plasma internal inductance l_i , line-averaged electron density n_e and volume-averaged electron temperature $\langle T_e \rangle$ versus time t .

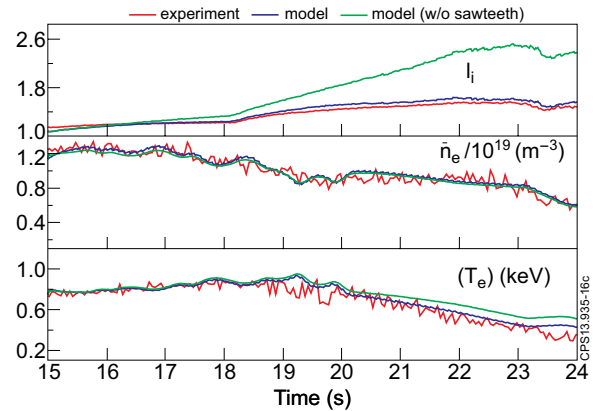


Figure 16: Model and experimental time traces for JET Pulse No: 77922 (comparing simulations with and without sawtooth model): plasma internal inductance l_i , line averaged electron density n_e and volume-averaged electron temperature $\langle T_e \rangle$ versus time t .

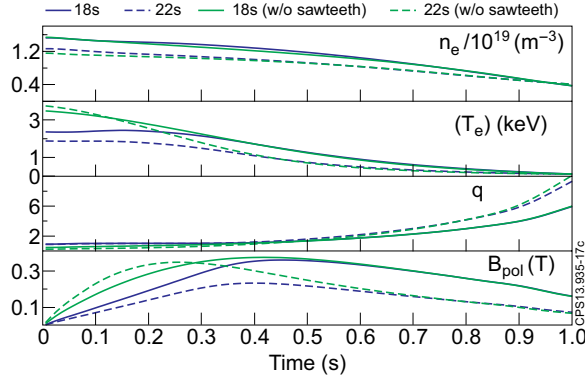


Figure 17: Model profiles for JET Pulse No: 77922 (comparing simulations before and during the current ramp, respectively at $t = 18\text{s}$ and $t = 22\text{s}$, with and without sawtooth model,): electron density n_e , electron temperature T_e , safety factor q and flux-surface averaged poloidal magnetic field B_{pol} versus flux coordinate ρ .

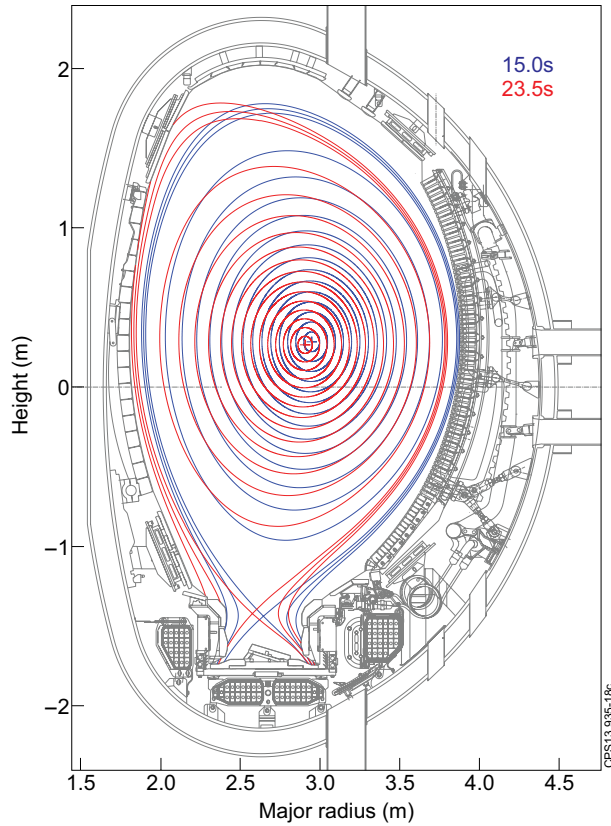


Figure 18: EFIT equilibria for JET Pulse No: 75225 at $t = 15.0\text{s}$ and $t = 23.5\text{s}$.